

## Flame spread over thin circular PMMA rods

Manu B V<sup>a\*</sup>, Amit Kumar<sup>a</sup>.

a. National Centre for Combustion Research and Development and Department of Aerospace Engineering, Indian Institute of Technology Madras, Chennai, India.

\* Corresponding author.

E-mail address: [ae19d017@smail.iitm.ac.in](mailto:ae19d017@smail.iitm.ac.in) (Manu B V).

### Abstract

This article presents a series of opposed flow flame spread experiments, conducted using cast cylindrical PMMA (acrylic) rods, 80 mm long and of diameters 1 mm and 0.5 mm, in normal gravity and microgravity environments. The experiments are primarily conducted for molar oxygen levels of 21%, 23% and 40% at 1 atmosphere pressure and opposed flow speed ranging from 0 cm/s to 25 cm/s. Experiments are also conducted in normal gravity for oxygen levels 21% to 60% to study the effect of oxygen level. At near ambient oxygen levels, the flame shape in microgravity resembles a mushroom and there are fluctuations at the leading edge due to sporadic fuel jets emanating from bursting bubbles at the fuel surface. The flame spreads faster in microgravity, which is determined to be due to increased preheat length. Preheat length is measured for flame spreading over 1 mm diameter fuel rod under no flow condition using fine thermocouples and is found to be 0.98 cm in microgravity and 0.34 cm in normal gravity. It is found that for scaling analysis, including Stefan flow velocity in the definition of reference velocity results in a reasonable estimate of the preheat length of a flame spreading in quiescent microgravity environment. At high oxygen levels ( $> 35\%$ ) the flame becomes turbulent and spreads at nearly the same rate in normal gravity and microgravity environments and the flame spread rates are not affected by external flow speed.

**Keywords:** opposed flame spread, thin circular PMMA rod, microgravity, oxygen effect, flame height, flame width.

### 1. Introduction

Fire safety in microgravity is important for ensuring safe human space missions. The spacecraft and its habitat are composed of various polymeric solid combustibles, which pose a risk of fire. Further, the spacecraft environment is very different from the earth's environment due to almost nil gravity, low convective flows and sometimes, lower pressure with elevated

oxygen [1]. Hence, combustion research and fire safety experiments in spacecraft environment are useful in providing deeper insight into the aspects of spacecraft fire safety. These experiments also provide useful data for validating the numerical and analytical models. The flame spread process over a solid surface involves preheating of fuel ahead of the flame, pyrolysis of solid fuel to form gaseous combustibles, which mix with air and react to form a self-sustained moving flame [2]. The flame spread over flat solid surfaces has been studied extensively and the progress has been periodically reviewed [3-5]. Flame spread along cylindrical fuels have received relatively less attention compared to the planar fuels and even lesser in microgravity conditions.

The earliest reduced gravity ( $10^{-2}g$ ) experiments on flame spread along PMMA rods were reported by Tarifa *et al.* [6] in 1990. Experiments were carried out on 1.5 mm, 2.0 mm and 2.5 mm diameter clear cast PMMA rods in quiescent oxygen rich (35% oxygen mass fraction) environment aboard KC-135. The PMMA rods burned vigorously with bright flame. It was reported that the flame spreads faster in reduced gravity compared to the normal gravity.

Bundy [7] in his thesis reported experiments aboard space shuttle on clear cast PMMA rods of diameter 2 mm and 6.4 mm. The experiments were conducted the quiescent microgravity at 50% oxygen concentration and the measure flame spread rates were found to be 3.11 mm/s for 2 mm diameter fuel rod and 0.78 mm/s for 6.4 mm fuel rod. The flames were bright yellow, with flares bursting in the radial direction from the fuel surface in both microgravity and normal gravity. The work also investigated the flame spread phenomena using CFD. It was reported that steady flame spread process does not occur in microgravity for fuel rods of diameter of 10 mm. Carmignani *et al.* [8] digitalised the VHS videos of PMMA experiments of SSCE [7] and by analysis showed that unlike planar fuel, the surface re-radiation has very little effect on extinction of flame over cylindrical fuels. Link *et al.* [9] conducted opposed flow flame spread tests aboard ISS on black cast PMMA cylindrical rods. The rod were 57.2 mm long and diameters were 6.4 mm, 9.5 mm and 12.7 mm. The opposed flow speeds was varied from 0.4 cm/s to 8 cm/s and the oxygen concentration was varied over a range 15% to 21%. The flame spread rate was reported non-monotonic increase-decrease variation with opposed flow speed. The maximum flame spread rate was noted for flow speed slightly below 2 cm/s. This trend is different from monotonic decreasing trend of flame spread rate with flow speed under normal gravity. No self-spreading flames were observed, as the flow speed decreased below 0.6 cm/s the flames extinguished. It was reported that for all rod diameters tested at  $X_{O_2} = 21\%$ , the

flame spread is faster in normal gravity than in microgravity. However, below  $X_{O_2} = 19\%$  the flame spread becomes faster in microgravity than in normal gravity. The rods were more flammable in microgravity and flame spread even at  $X_{O_2} = 17\%$ , while the flame extinguished in normal gravity for  $X_{O_2} = 18\%$  and below. Wu *et al.* [10] conducted the flame spread experiments on extruded clear PMMA rods with 10 mm diameter in the SJ 10 Satellite. The opposed flame spread behaviours were studied at the oxygen enriched ambient (33.5% and 49.4%) under low flow speeds in the range of 0~12 cm/s. Interestingly, the flame spread rate was reported to increase with increase in opposed flow speed. This trend was attributed to the decrease in flame standoff distance, which in turn results in enhanced heat flux at the fuel surface. The microgravity flame spread rates in oxygen enriched atmosphere were of the order of 0.1 mm/s. This is about one fifth to one tenth of the flame spread rate in normal gravity at the same nominal opposed flow speed. In microgravity the change in the flame spread rate due to oxygen enrichment (from 21% to 50%) was about 2-3 times, where as in normal gravity the flame spread rate increase was noted to be more than 10 times. In microgravity the flame sheet had blue hue and was marked with frequent burst of bubbles.

Compared to microgravity studies, there are relatively more flame spread studies on cylindrical rod fuels in normal gravity. In an early work, Sibulkin and Lee [11] conducted experiments on PMMA cylinders of diameters ranging from 1.6 mm to 12 mm and with fuel orientation ranging from  $-90^\circ$  (downward propagation) to  $+40^\circ$ . Temperatures were measured at different locations of solid and gas phases and an energy balance analysis was carried out primarily for a downward spreading flame. For a 12.7 mm PMMA cylinder it was estimated that around 40% of heat feedback to unburnt fuel ahead of the flame is by conduction inside the solid and 60% is due to surface heat transfer. Also, only 6% of heat of combustion is return back to fuel rod and after losses only 1% is responsible for the propagation of the flame propagation. Fernandez Pello and Santoro [12] conducted experiments on opposed flow flame spread along PMMA rods of 1.6 mm and 50 mm diameters in normal gravity. Temperature measurement in solid and gas phases showed that, the dominant mode of heat transfer to the fuel ahead of the flame is a function of diameter of the cylinder. While the gas phase conduction was found to be more important at smaller fuel diameter, conduction through solid cylinders increases at large fuel diameter and controls the flame spread. Huang *et al.* [13] conducted the flame spread experiments on 3.2 mm, 6.4 mm, 9.5 mm, and 12.7 mm cast black PMMA rods at various flow speeds in normal gravity. The flame spread rates were not affected by flow speeds below 30 cm/s flow. As flow speed increases, the flame spread mode transformed into fuel regression

mode at around 50 cm/s to 100 cm/s of opposed flow and subsequently extinguished at much higher flow speed. Thomsen *et al.* [14] conducted the low pressure flame spread experiments (100 kPa to 30 kPa) on 12.7 mm, 9.5 mm, and 6.4 mm diameter cast black PMMA rods to simulate reduced gravity affects by reducing buoyancy. The flame shapes were compared with those in microgravity [9]. At low pressures, the opposed flow spreading flame over thick PMMA rods becomes shorter, dimmer and spreads at lower spread rates. Further reduction in pressure forms a rounder blue colour flame similar to the flames observed in microgravity. It was concluded that simulating opposed flow flame spread in microgravity by reducing pressure, might be considered only an approximate as the flow characteristics in reduced buoyancy are still different from microgravity flow and pressure also influences chemical kinetics. Thomsen *et al.* [15] conducted normal gravity experiments on 12.7 mm, 9.5 mm, and 6.4 mm diameter cast black PMMA rods at ambient pressures ranging between 100 and 60 kPa and oxygen concentrations between 21% and 35% by volume, while maintaining normoxic conditions (same oxygen partial pressure). It was noted that as the pressure is reduced the flame becomes longer and spreads faster. Korobeinichev *et al.* [16] conducted the experimental study of downward flame spread over single pine needles of 0.6 mm  $\times$  1 mm cross section in normal gravity. Detailed chemical and thermal structure of the flame are obtained by measuring species concentration in gas phase and temperature field in gas and solid phases. Naresh *et al.* [17] numerically simulated the flame spread experiments on pine needles conducted by Korobeinichev *et al.* [16]. Here the pine needles are treated as thin cellulose cylinders of 0.8 mm diameter and a 2D axisymmetric numerical model with char formation and oxidation is developed to simulate the flame spread process. The simulated flame spread process agrees well with the experiments.

In addition to experiments, over the years researchers have developed analytical models to explain underlying mechanisms of flame spread and predict the opposed flame spread rate along rods of cylindrical cross-section. These models stem from the classical model of flame spread of De Ris for opposed flame spread over a flat fuel [19]. The semi empirical model of Delichatsios [20] accounted for heat flux enhancement due to curvature effects. The model thus enables prediction of flame spread rate along cylindrical rods based of flame spread data over same fuel in flat geometry. Bhattacharjee and Delzeit [21] proposed a scale-based model for cylindrical fuels in thermally thin and thick limits. Further improvements in the model have enabled prediction of flame spread over electrical wires including conduction in the core metal,

dripping of insulation material [22] and the radiation extinction at low opposed flow speeds [23].

From the above literature survey, one can note that there is little data available in thermally thin cylindrical rods in both normal gravity and microgravity. In fact, there is no experimental data on flame spread for a thin circular rods less than 1.5 mm diameter. Therefore, the present work aims to study the opposed flow flame spread behaviour along thin circular cylindrical rods in both normal and micro gravity environments at various oxygen concentrations and oxidiser flow speeds.

## 2. Casting of cylindrical PMMA rods

The commercially available PMMA rods of small diameters (here below 12 mm) are manufactured by extrusion. The extruded PMMA, unlike cast ones have shorter molecular chains which results in melting and dripping during the burning process. Therefore, to obtain cast PMMA rods of small diameters, the samples are either machined from a larger diameter samples or cast directly. However, for small diameters of about 1 mm, machining becomes challenging and fuel length also gets restricted [6]. Therefore, in this work the sub-millimetre diameter acrylic (PMMA) rods are cast using standard melting point capillaries (available locally with ID of 1 mm and 0.5 mm). Non-standard capillaries formed by glass blowing were also tried to obtain cast of diameters 1.5 mm and above. However, due to non-uniformity in diameter and non-repeatable production, these were discontinued. The cast samples made here are clear cylindrical PMMA rods, typically 80 mm long, and diameters 1 mm, and 0.5 mm. The cast rods are produced by the polymerization of MMA (Methyl Methacrylate) monomer using a BP (Benzoyl Peroxide) as polymerizing agent in 10:1 ratio by weight. This solution of MMA+BP is activated by heating it to 90°C in a hot air oven. The viscous activated liquid is filled into 100 mm long melting point glass capillaries of 1 mm or 0.5 mm ID. The filled capillaries are sealed at the ends by thermoset glue and let to cure in a hot water bath. The hot water bath is maintained at 33°C for the first 12 hours, followed by 36 hours at 36°C and then for another 48 hours at 50°C. This program of gradual increase in water bath temperature, aided with forced convection, enhances heat removal from the tubes, and thus avoid bubble formation during the polymerization process. This schedule of the heating process is arrived at based on trial and error to obtain bubble-free cast PMMA rods. Figure 1 illustrates the above mentioned steps of making clear cast cylindrical PMMA rods.

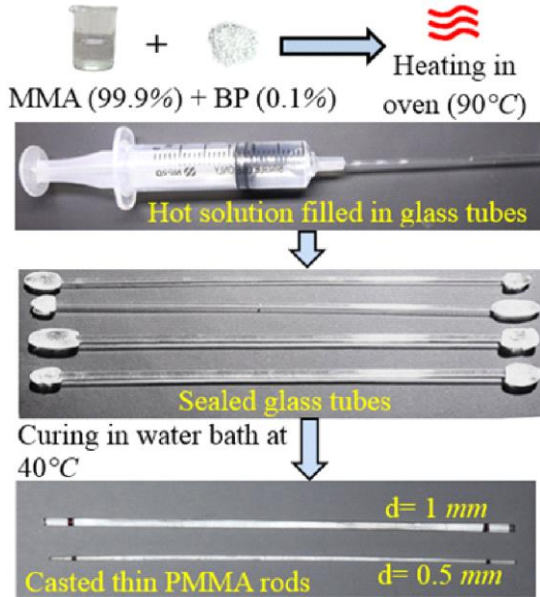


**Fig. 1.** Casting of thin circular PMMA rods/cylinders.

### 3. Experimental setup

The experimental setup consists of two main parts, a combustion tunnel and an enclosure (see Fig. 2(a)). The combustion tunnel is a duct of square cross-section with inner dimensions of 12 cm x 12 cm and height 54 cm. It comprises of an upper transparent polycarbonate test section of height 25 cm and a flow conditioning unit, 29 cm high. The test section houses a sample holder, an ignition coil, and mountings for cameras and thermocouples. The sample holder is 80 mm long, thin stainless steel capillary tube of 1.2 mm ID and 1.5 mm OD attached to a thin stainless steel strip 10 mm wide and thickness of 0.5 mm. The metal strip spans along the width of the test section (see Fig. 2(a)) facilitates holding of fuel samples vertically and aligned to the flow direction with minimum flow disturbance. The ignition coil is a 15 turn spiral of 6 mm ID and length 20 mm. The ignition coil is made of 24 gauge (0.55 mm diameter) Nichrome wire, which is energized by a 24 V DC source. The flow conditioning unit (see Fig. 2(b)) of the combustion tunnel is a modular stainless steel duct comprises of a 12 V DC fan at the bottom, followed by a 25 mm long section of honeycomb flow straightener with channel diameter of about 4 mm, and lastly a 100 micron stainless steel mesh, to get the required uniform laminar flow. The flow speed is varied by controlling a supply voltage to the fan using a voltage regulator. The flow speed is measured at a plane located at the centre of the test section, by using a one directional hot wire anemometer (TSI-9535). The complete combustion tunnel is enclosed within an airtight 44 litre outer polycarbonate enclosure with

provision for inlet and outlet to fill and exhaust the gases (oxygen and nitrogen) to set an environment of desired oxygen concentration.

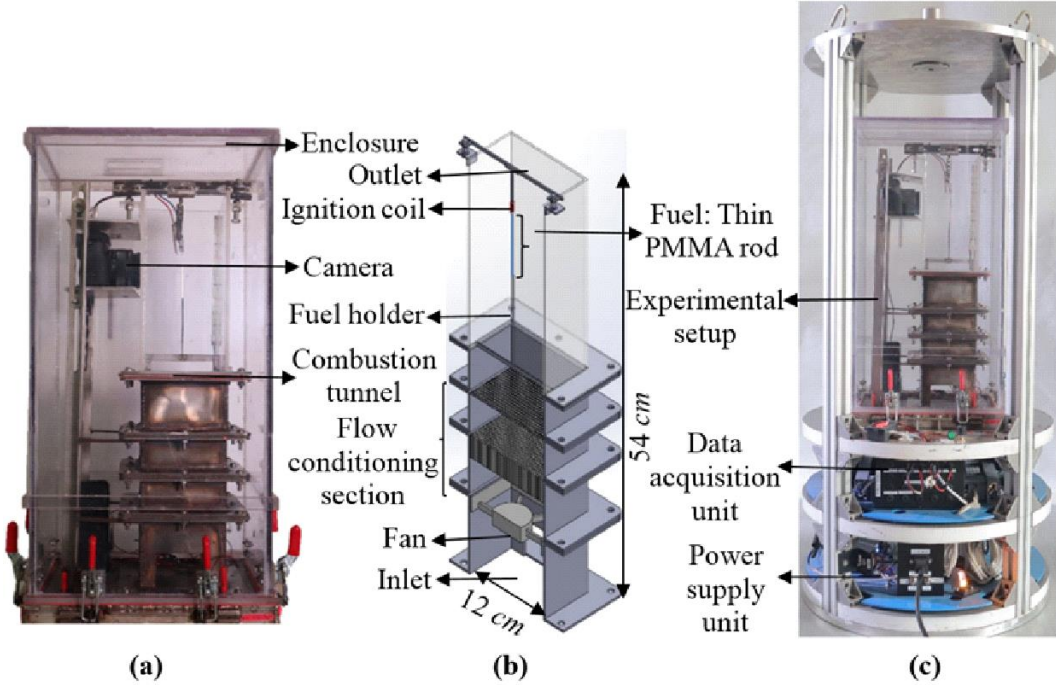


**Fig. 2.** (a) Photograph of the experimental setup, (b) Schematic of the combustion tunnel, and (c) Photograph of microgravity drop capsule.

The microgravity experiments are carried out in 2.5 s microgravity drop tower located at IIT Madras [24]. The experimental setup used for the microgravity experiments is the same as used for the normal gravity experiments as shown in Fig. 2(a, b). The drop capsule (see Fig. 2(c)) for the microgravity experiment is provided with necessary space for accommodating the entire experimental setup along with control unit and data acquisition system for operation of the experiment. There is a power supply system to power all the power consuming instruments on board the drop capsule.

The flame spread process at both normal and microgravity conditions is captured using a Canon M50 Mark 2 digital camera at rate of 50 FPS. The flame spread rate is obtained by tracking a leading edge of a flame. The shape and growth of flame is characterised by tracking a height and width of the spreading flame by using an in house image processing algorithm called Flame Spread Analyser (FSA) developed in MATLAB.

For select experiments temperature of the gas phase adjacent to the PMMA surface is measured by using a 50  $\mu\text{m}$  S-type (Platinum Rhodium 10% - Platinum) thermocouples at sampling rate

of 50 Hz with NI-9213 data acquisition system. The thermocouples are placed at different axial and radial locations, the details of which are discussed in section 4.2. The Schlieren imaging, and shadowgraphs in normal gravity are done using a LAVISION-FASTCAM-SA 1.1 high speed camera at 1000 FPS with normal and zoom lenses respectively. Simultaneous high-speed imaging of the normal gravity flames is done using IDT-NXA4S3 camera at 1000 FPS. The burnt cones are examined using an Amscope digital microscope and imaged using a MD500 digital camera at 80X magnification.

#### **4. Results and discussion**

Experiments are carried out on cast PMMA rods of circular cross section of diameters, which varied from 0.5 mm to 10 mm. Since there is no available data for small diameters below 1.5 mm, the focus of this study is more on the thin circular rods, specifically of diameters 1 mm and 0.5 mm. Limited tests are carried out for other larger fuel diameters for verification of present data with the already available data in the literature. For the thin fuels (here 1 mm and 0.5 mm diameter), experiments are carried out in both normal gravity and microgravity environments. The oxygen levels in the experiments are 21%, 23% and 40%. Selected experiments in normal gravity are also carried out at various other oxygen levels in the range 21% to 60%. The externally imposed opposed flow speeds is also varied in the experiments over the range 0 cm/s to 25 cm/s, in steps of 5 cm/s.

In the following section flame spread over circular rods in normal gravity and microgravity in ambient atmosphere of 21% oxygen and 1 atmosphere pressure is discussed. Effect of flow speed on flame spread rate is examined for 1 mm and 0.5 mm diameter fuel rods. Next the effect of oxygen level is examined largely in the absence of an external flow. Following this flame spread rate data at various flow speeds, oxygen levels and fuel diameters obtained in the present study is summarised along with similar data form other previous studies.

##### **4.1 Effect of flow speed on flame spread in normal gravity and microgravity**

Experiments are first carried out for various fuel diameters in normal gravity and microgravity environments at atmospheric conditions of 21% oxygen and 1 atmosphere pressure. Figure 3 shows instantaneous images of spreading flame in normal gravity (Fig. 3(a)) and in microgravity (Fig. 3(b)) for fuel diameters from 0.5 mm to 10 mm. In normal gravity, the flames are slender and laminar and their length are seen to increase with increase in fuel diameter. In microgravity there is drastic change in flame shape, they are wider due to

absence of inward induced flow due to buoyancy. For small diameters (0.5 mm, 1 mm, and 1.5 mm) the flames are longer and wider than their normal gravity counterparts and for larger diameters (6 mm and 10 mm), flames have become shorter and wider than corresponding normal gravity flames. Since the microgravity test duration is short (2.5 s), the flames are still growing.

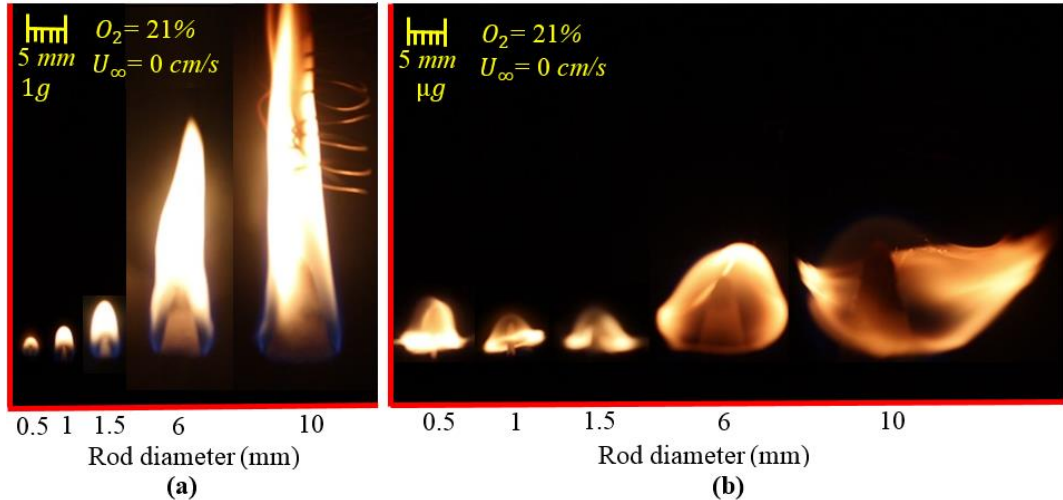


**Fig. 3.** Instantaneous front view images of spreading flame along circular PMMA rods of various diameters in (a) normal gravity, (b) quiescent microgravity at 2.5 s after the drop.

During the microgravity test duration, while a clear movement of flame front is observed for fuels of diameter 1.5 mm or lesser, the flame front is nearly stationary for 6 mm and 10 mm fuel diameters. Further microgravity tests with forced convective flow are carried out only on 1 mm and 0.5 mm fuel diameters. Figure 4 shows instantaneous images of spreading flames in normal gravity (top) and microgravity (down), along 1 mm and 0.5 mm diameter fuel rods at three external flow speeds, namely, no external flow (0 cm/s), 10 cm/s, and 25 cm/s. Oxygen level is 21% and pressure is 1 atmosphere. The normal gravity flames are laminar with blue leading edge followed by orange-yellow extent downstream. Flames over 0.5 mm fuel have length (h) and width (w) are nearly same giving them a spherical appearance. Flames over 1 mm cylinder are taller and have higher aspect ratio (h/w). With increase in external opposed flow speed the flame is seen to become shorter for both 0.5 mm and 1 mm diameter fuel rods.

The flames in microgravity have a typical ‘mushroom shape’ appearance, are less intense and orange in colour. The flames are larger compared to the normal gravity flames. The bottom of the flame is marked with random fluctuations due to pyrolysate jet emanating from bursting bubbles formed inside the PMMA rod. With an increase in the flow speed the flame size

reduces in both height and width and at high flow speed of 25 cm/s they tend to look similar to normal gravity flame. The fluctuations at the flame leading edge is also seen to reduce with increase in flow speed probably due increase in stream wise momentum. It may also be noted

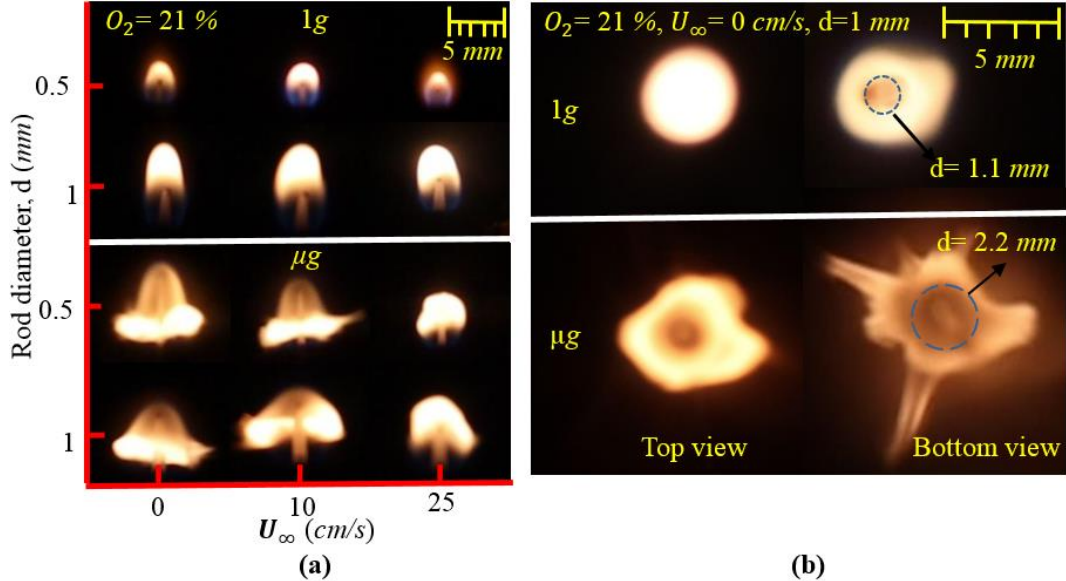


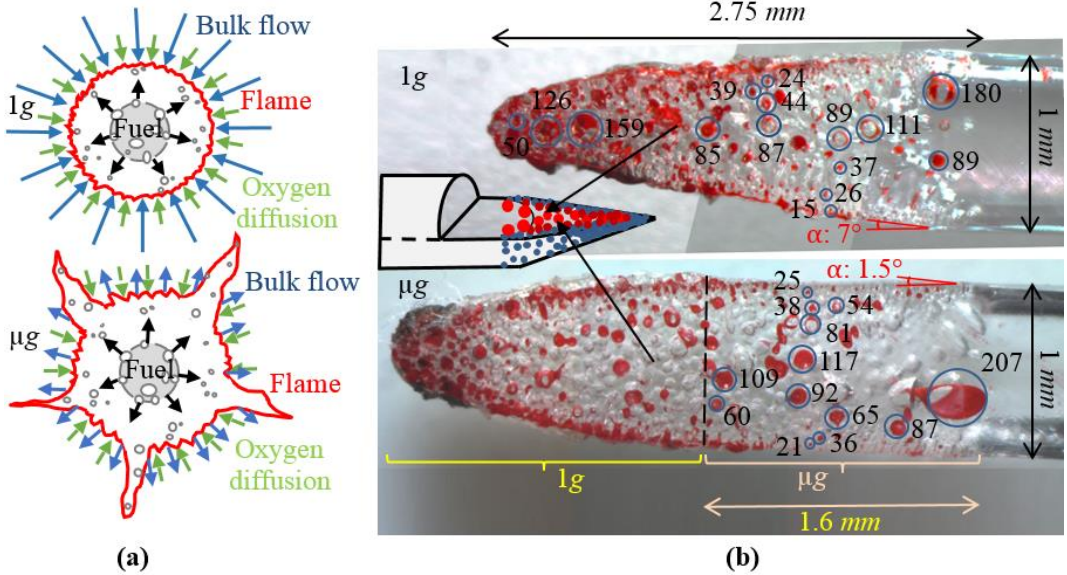
**Fig. 4.** (a) Instantaneous front view images of spreading flame along fine PMMA rods of diameter 1 mm and 0.5 mm in normal gravity and microgravity at various opposed flow speeds, (b) Top and bottom views of flame for 1 mm diameter PMMA rod with no external flow.

that bursts of fuel jet are seen only at the flame leading edge where the fuel (PMMA) is still hard. As the fuel gets softened and fuel jets are much less intense for visual observation. Figure 4(b) shows the top and bottom views of flame spreading over 1 mm diameter fuel rod in normal gravity (upper sub figure) and quiescent microgravity (lower sub figure) environments. These images of the flame are taken from top and bottom of the burning fuel to get an azimuthal view of the flame and the fluctuations. The fuel is placed vertically on top of a clear polycarbonate plate without sample holder to get an unobstructed view of the flame. The bottom end of the fuel rod is carefully stuck on to the plate top using a small amount of instant glue. The experiments are conducted in both normal gravity and microgravity for condition of no external flow. The top and bottom views of the normal gravity flame shows near perfect circular shape with minor distortions. For the microgravity flame, the top and the bottom views show distortion of circular shape due to sporadic fuel jets. The streaks of flame coming out can be clearly seen in the bottom view are due to fuel jets from bursting bubbles. Note that the camera settings are different in the top and bottom views to capture the desired feature of the flame. The visible streaks of fuel jets are seen to traverse radial distance of the order of 5 mm. It is

interesting that while bubble formation is present during both normal gravity and microgravity flame spread process the distortion of flame is visibly prominent in microgravity. This could possibly be due to suppression of fuel jet momentum by opposing momentum of radially inward buoyancy induced flow of air in normal gravity. In quiescent microgravity environment there is no opposing momentum of air. This is illustrated by sketch in Fig. 5(a). The fuel jet streaks have also been noted by the researchers in their low pressure combustion study of PMMA rods [14-15]. The frequency of sporadic radial fuel jets released due to bursting of bubble is decreases for larger fuel diameters [15].

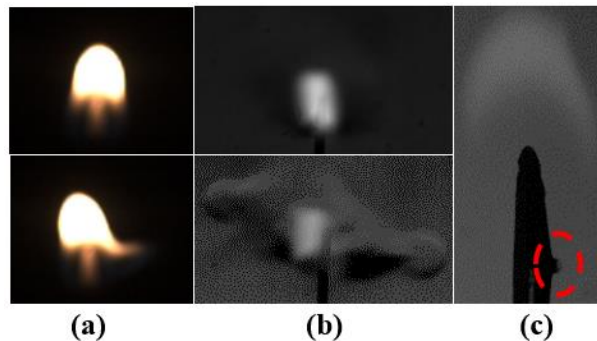
Similar distortion of flame shape by release of fuel vapour by bursting of bubbles in the solid fuel and ejection of material itself by bursting of bubbles in a combustion of polymer spheres in reduced gravity is observed [18]. Here reduced gravity combustion experiments are carried out for polymethylmethacrylate (PMMA), polypropylene (PP), and polystyrene (PS) spheres of diameters ranging from 2 mm to 6.35 mm with varying the oxygen concentration from 19% to 30% and pressure from 0.05 MPa to 0.15 MPa. Here in normal gravity, initially all spheres diameter increase due to swelling. Subsequently materials stars dripping and diameter reduces. In case of micro gravity, initially diameter of spheres increases by swelling similar to normal gravity. In addition the flame shape distorts by release of fuel vapour by bursting of fuel bubbles and in case of polypropylene spheres material itself ejects out of flame zone and traverse around 8 mm from the sphere surface before complete combustion. Here, in the present study, the distortion of flame shape by release of fuel vapour by bursting of bubbles is observed and the ejection of material by bursting of bubbles and swelling of cylinders are not observed.

Figure 5(b) shows the magnified images (80X) of the burnt PMMA samples from normal gravity (upper sub figure) and microgravity (lower sub figure) tests. The burnt samples show bubbles spread over entire pyrolysis region and to some extent in depth of the preheat region. In normal gravity, the pyrolysis segment is conical in shape with cone tip half angle of about  $7^\circ$ . The quiescent microgravity flame spread is obtained by igniting fuel first in normal gravity and then conducting the drop test after about 25 s for 1 mm diameter fuel rod. Marked on the image in Fig. 5(b) is the segment of the pyrolysis region over which the flame spreads during the microgravity test duration. One can note that the angle the pyrolysis surface makes with the axis is much shallower (here about  $1.5^\circ$ ) than in normal gravity. In microgravity tests on thick PMMA rods of diameter 1.27 cm in space station [13] this angle was found to be about  $5^\circ$ . The corresponding angle in normal gravity for the same sample was about  $20^\circ$ .



**Fig. 5.** Schematic illustrating flame distortion at flame leading edge due to bursting bubbles at normal gravity and microgravity, (b) Magnified mid plane view of burned thin PMMA rod (1 mm diameter) in normal and microgravity.

In order to look at the in-depth distribution of bubbles in the pyrolysis region, the burnt samples were cut longitudinally at the mid plane as shown by the sketch in Fig. 5(b). To distinguish open bubbles in mid plane from the bubbles in the back ground, a red dye dissolved in alcohol was used to fill the open bubbles. One can note small numerous bubbles occupy the region close to the surface of fuel and larger bubbles are seen deeper inside the solid fuel. More number of large bubbles are seen in microgravity especially near the preheat region. The in-depth shape of the pyrolysis front also looks different compared to the deeply concave pyrolysis front in normal gravity.



**Fig. 6.** High speed images showing occasional large bubble burst in normal gravity, (a) colour image, (b) Schlieren image, and (c) shadowgraph with zoom lens shows bursting bubble at the fuel surface.

As mentioned above there are trapped bubbles in the solid PMMA even for the normal gravity flame, however the flame shape is not distorted by the fuel jets from the bursting bubbles. The normal gravity flames over 1 mm fuel diameter were observed directly with high speed imaging using IDT-NXA4S3, schlieren and shadowgraph imaging using LAVISION-FASTCAM-SA 1.1 high speed camera at 1000 fps. The normal gravity flame appears smooth in these images as well except for occasional (4-5 times during the complete burning of the fuel rod) burst of fuel jet. Figure 6. shows images of visible flame (Fig 6(a)), Schlieren image (Fig. 6(b)) and shadow graph (Fig. 6(c)) of such an occurrence. These incidents last for about 10 ms, hence not observable to the naked eye.

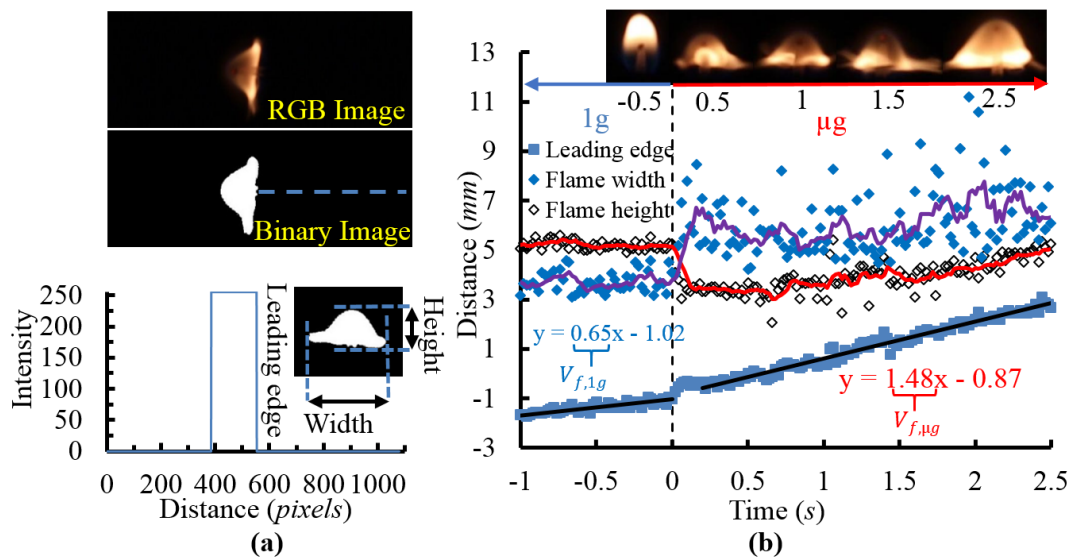


**Fig. 7.** (a) Typical RGB image of microgravity flame (at 21% O<sub>2</sub> and 0 cm/s flow speed), processed binary image, measured flame dimensions and flame leading edge tracking position, (b) Variation of flame leading edge position, flame height and flame width with time.

The videos of the spreading flames in normal gravity and microgravity are captured using Canon M50 II DSLR camera at 50 fps. The flame spread rate ( $V_f$ ) and geometrical parameters of flame (height (h) and width (w)) are obtained by processing the individual frames extracted from the video. The RGB frames extracted from the video are converted into binary (black and white) images using Otsu's method [25] of thresholding. The threshold value is obtained for each image to account for the continuous change of flame intensity in the transient phase of flame growth especially in the case of microgravity flame spread. Figure 7(a) illustrates a typical RGB image of a microgravity flame at 21% O<sub>2</sub> and 0 cm/s free stream flow speed and its corresponding binary image after thresholding. The measured geometrical dimensions of the flame are also indicated in Fig. 7(a). The height of the flame is obtained by tracking the

trailing and leading edges of a flame at the centre of the fuel and width is tracked at the location of maximum width. The flame spread rate is obtained by tracking the flame leading edge (see bottom sub figure in Fig. 7(a)) along the solid fuel in pixels and converted into physical distance. In a typical image, for 1 mm distance there are 17 pixels. Figure 7(b) shows measured flame width (w), height (h) and leading-edge position at various instants of time. For time,  $t < 0$  s represents data in normal gravity,  $t = 0$  s is the initiation of the drop test and  $0 < t < 2.5$  s is the data of flame spread over the duration of microgravity. Also shown in Fig. 7(b) is the instantaneous images of flame at selected time instants of the microgravity test duration.

In Fig. 7(b), on either side of  $t = 0$  s, the position of the flame leading edge with time appears to follow a straight line, which implies a steadily spreading flame. The slope of the least square linear fit gives the steady flame spread rate ( $V_f$ ). One can note the slope and hence the flame spread rate is higher in microgravity (1.48 mm/s) compared to normal gravity (0.65 mm/s). It is interesting to note a sudden upstream jump in flame leading edge position at the start of the drop test. This is due sudden removal of buoyant force on the flame directed in the downstream direction. As far as the flame dimensions are concerned, in normal gravity the flame height is more than the flame width (an aspect ratio,  $h/w$  of 1.4). However, at the start of the drop test there is a sudden increase in the width of the flame, and simultaneously flame shrinks in height resulting in complete change of flame aspect ratio ( $h/w \sim 0.48$ ). Both the flame width and the flame height are seen to increase with the passage of time during the microgravity test duration. The flame as a whole is seen to increase in size. The flame aspect ratio also appears to vary marginally from about 0.48 at the start of the drop to 0.56 at the end of the drop (about 17% change). In the drop tower experiments of Olson [26] it was also noted that while the flame spread at a steady rate, the flame shape was still evolving.

The variation of flame height (h) and flame width (w) with flow speed in both normal gravity and microgravity is shown in Fig. 8. Figure 8(a) shows this variation for fuel diameter of 1 mm and Fig. 8(b) for fuel diameter of 0.5 mm. In the two sub figures, the microgravity flame dimensions (h and w) are represented by solid curves and normal gravity flame dimensions are represented by dashed curves. Note that the microgravity flame dimensions here are taken at time of 2.46 s just before the end of the drop test. As mentioned earlier, for the forced flow speed of 0 cm/s, the microgravity flames have aspect ratio  $h/w < 1$ , and as the flow speed is increased the aspect ratio value appears to increase towards unity.

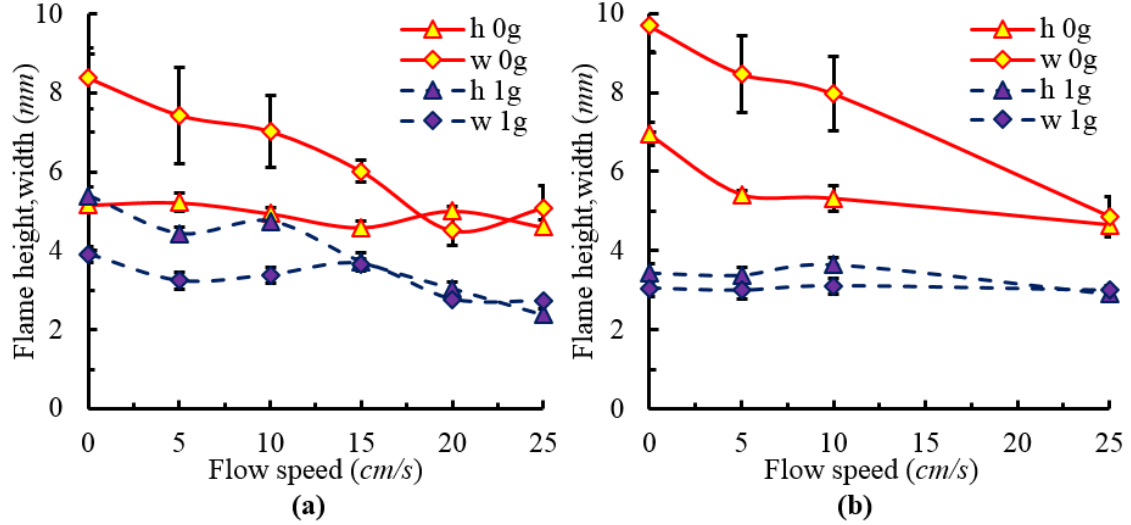


**Fig. 8.** Variation of flame height and flame width with flow speed in normal and microgravity at 21% oxygen, (a) 1 mm diameter rod, (b) 0.5 mm rod.

It may be noted that at low flow speeds, the slope of curve of flame width with flow speed is higher than the slope of curve of flame height with higher flow speed. On the other hand in the normal gravity, the flame aspect ratio,  $h/w > 1$  and as the flow speed increases the flame aspect ratio decreases and is also seen to approach unity. Here in normal gravity, the slope of curve for flame height is somewhat steeper than the slope of curve for flame width. In Fig. 8(b), for the fuel diameter of 0.5 mm, in microgravity, the flame widths and heights are noted to be wider than the corresponding flame for 1 mm diameter fuel. The flame aspect ratio for the flow speed of 0 cm/s increases from 0.63 at the beginning of the drop test to 0.77 at end of the drop test. The spreading flames over 0.5 mm fuel diameter in normal gravity on the other hand are shorter and narrower compared to the flames over 1 mm diameter fuel under same flow conditions. From these experiments, it appears that flow has stronger influence on flame width in microgravity and flame height than in normal gravity. Both flame width and flame height decrease with increase in flow speed in microgravity as well as normal gravity.

The variation of the flame spread rate with flow speed for 1 mm and 0.5 mm diameter fuels is shown in Fig. 9. In general, flame spread rates in microgravity are higher than corresponding flame spread rates in normal gravity and the flame spread rate decreases with increase in flow speed in both normal gravity and microgravity. However, the slope of the curves are steeper in microgravity compared to that for the normal gravity flames. It is interesting to note that present decreasing flame spread trend with flow speed is unlike non-monotonic flame spread trend with flow speed that have been reported [9]. Note that, in [9] non-monotonic spread rate with

flow was reported with maximum spread rate at around 2 cm/s of flow speed. In present work due to starting inertia of the fan, the minimum flow speed is limited to 5 cm/s.

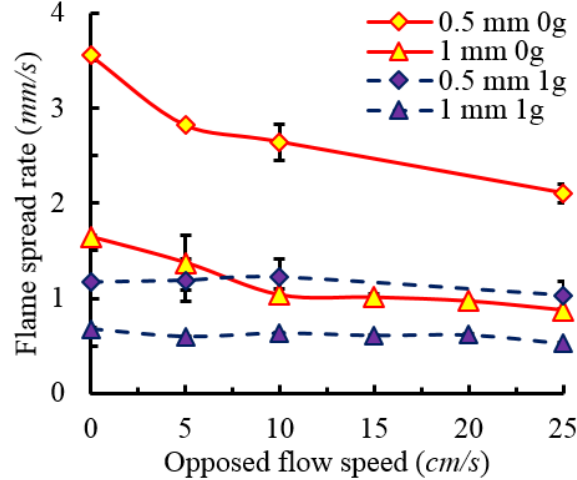


**Fig. 9.** Variation of flame spread rate with flow speed at normal and microgravity at 21% oxygen.

#### 4.2 Flame temperature measurement and the preheat length

It is interesting to note that the microgravity flame especially at low flow speeds appear to have a significantly increased flame standoff distance at the leading edge (see Fig. 4) and yet the flame spread rate is significantly higher than the corresponding normal gravity flame spread rate. In order to understand the reason, flame temperature measurements were carried out on spreading flames along 1 mm diameter fuel rods in both normal gravity and microgravity at 21% oxygen level and no forced flow condition to get a measurement of the preheat length. Temperatures are measured using 50  $\mu$ m S type (Pt with Pt-Rh 10%) thermocouples. Figure 10 presents a typical measured thermocouple data in normal gravity (Fig. 10(a)) and microgravity (Fig. 10(b)).

Figure. 10(a) also shows a schematic of thermocouple located at an arbitrary position ahead of the flame leading edge (say at time  $t = 0$  s). The thermocouple is at a radial distance of 0.2 mm from the fuel surface (at 0.7 mm from the axis of 1 mm diameter fuel rod). As the flame spreads, it approaches the thermocouple at the rate of flame spread rate ( $V_f$ ) the temperature of the thermocouple rises to a maximum and then drops after the passage of the flame. In the inset flame image, the vertical dashed line indicates the thermocouple position engulfed in flame.

The flame temperature at this time is indicated by intersection of red line with the temperature curve.

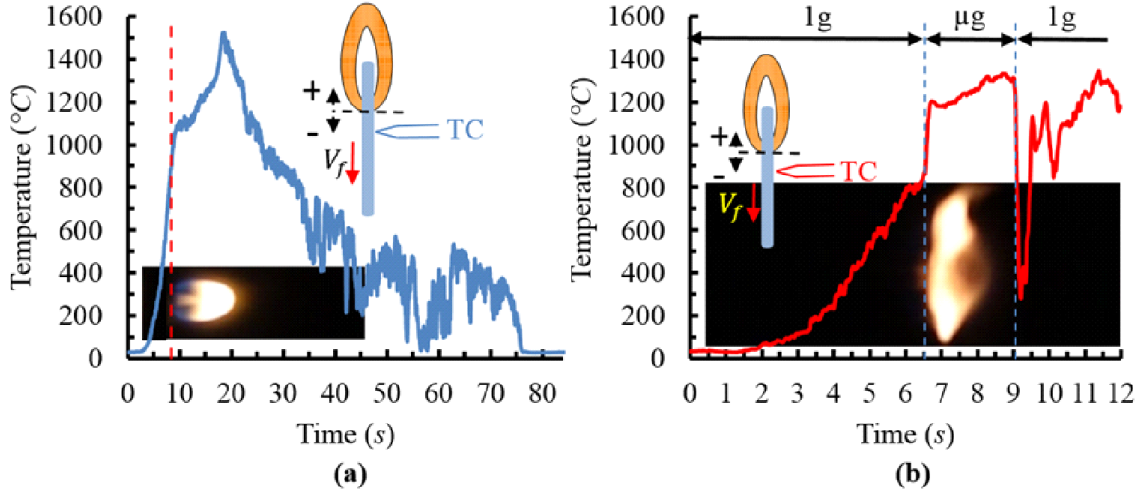


**Fig 10.** Temporal variation of measured temperature from a stationary thermocouple as flame spreads along PMMA rod of diameter 1 mm, (a) normal gravity, (b) micro gravity, Oxygen level is 21% and no forced flow.

Similar to Fig. 10(a), Fig. 10(b) shows a schematic of thermocouple located at an arbitrary position ahead of the flame leading edge for a microgravity flame spread. The thermocouple is at a radial distance of 2 mm from the fuel surface (2.5 mm from the axis of the 1 mm diameter fuel rod). Note that the fuel is ignited in normal gravity and as flame spreads and reaches desired position of the thermocouple in relation to the flame leading edge, the drop test is initiated. Therefore, unlike Fig. 10(a), here only a part of measured temperature curve (for a duration of 2.5 s) is in microgravity. The segment of flame spread curve in microgravity is bounded by two vertical dashed lines as shown in Fig. 10(b). The rest of the temperature data before the drop test and after the end of the drop test corresponds to the temperature of the spreading flame in normal gravity and hyper gravity (during deceleration).

Since the flame spread rate is steady, the temporal variation of measured flame temperature shown in Fig. 10 can be transformed into flame temperature variation in spatial coordinates using  $ds = V_f dt$ , where  $ds$  is the small distance leading edge of the flame traverses during the time interval of  $dt$ . Figure 11 shows the spatial variation of the flame temperature in normal gravity (Fig. 11(a)) and in microgravity (Fig. 11(b)), obtained using the steady flame spread rate values ( $V_f$ ) and data in Fig. 10.

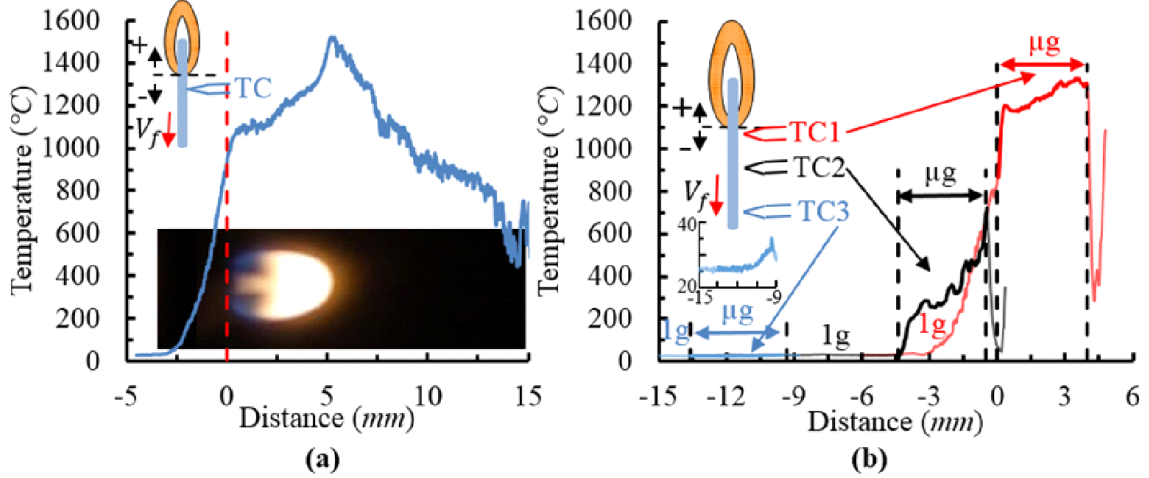


**Fig. 11.** Temperature variation along the axial direction for the case of no forced flow and 21% oxygen in (a) normal gravity, (b) micro gravity.

In normal gravity, for 1 mm fuel diameter at 21% oxygen level and no forced flow condition, the flame spreads at the rate of 0.68 mm/s and that in microgravity it spreads at rate of 1.65 mm/s. Note that, in obtaining spatial variation of temperature in Fig 11(b) flame spread rate in microgravity is used for the duration in microgravity and for rest of the duration spread in normal gravity is used.

For the microgravity duration of 2.5 s at a flame spread rate of 1.65 mm/s, the spatial distance covered in microgravity is only about 4 mm. Therefore, to obtain larger coverage of spatial temperature profile, three thermocouples (TC1, TC2, and TC3) positioned at different axial locations and fixed radial location are used in one drop test. The schematic in Fig. 11(b) shows the position of the three thermocouples. Here the distance between TC1 and TC2 is 4.5 mm and that between TC2 and TC3 is 8.5 mm. The temperature measured by these thermocouples are also shown in three different colours. The measured temperatures curves show both normal gravity and microgravity durations (portions bounded by vertical dashed lines). A segmented spatial temperature profile in microgravity is thus obtained. The experiments are repeated with change only in the axial position of the thermocouples with respect to flame leading edge just before the start of the drop test. This was achieved using a timer relay to control time of the start of the drop test. The microgravity flame temperature data from different experiments are stitched together to get a more complete spatial flame temperature profile in microgravity. It may be noted here that thermocouple (TC3), which in this case is 13 mm upstream of TC1, shows an increase in temperature towards the end of the microgravity temperature profile segment measured by it (please see inset figure in Fig. 11(b)). Similarly, the end of

microgravity temperature profile segment of TC2 and the beginning of temperature profile segment of TC1 represent the position of the flame leading edge. With these data one can obtain an estimate of the preheat length of the spreading microgravity flame.

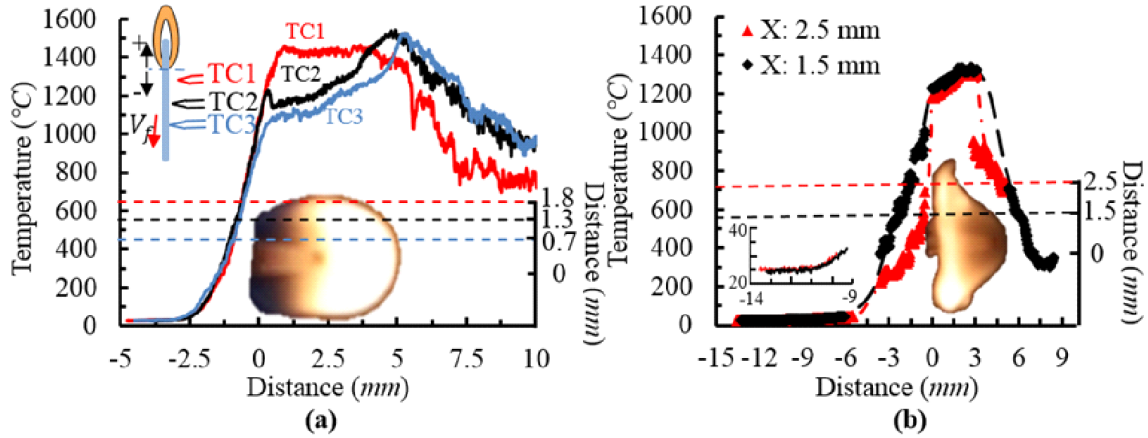


**Fig. 12.** Spatial variation of temperature along the flame spread or axial direction at different fixed radial locations in (a) normal gravity, (b) micro gravity. There is no forced flow and oxygen is 21%.

Figure 12 shows the spatial variation of temperature along the flame spread direction at different fixed radial locations in normal gravity (Fig. 12(a)) and microgravity (Fig. 12(b)). For normal gravity, in addition to thermocouple radial location of 0.7 mm from the axis (shown in Fig. 11(a)), the measured temperature profiles are shown for radial positions 1.3 mm and 1.8 mm from the axis of the fuel. In microgravity, the temperature profiles are piece wise combination of measured temperature segments at different axial locations with thermocouple radial positions of 2.5 mm and 1.5 mm from the axis of the fuel of diameter 1 mm. The radial position of the thermocouples with respect to flames is also shown in Fig. 12 as dashed lines parallel to the fuel axis.

In Fig. 12(a) the temperature variation along the axis parallel to fuel rod at radial distances of 0.7 mm, 1.3 mm, and 1.8 mm from the centre of the fuel rod for a normal gravity flame is shown. The thermocouple TC1 is at radial distance of 1.8 mm and it passes along close to the flame surface and records nearly constant temperature of around 1400 °C. The thermocouple TC2 and thermocouple TC3 are at radial distance of 1.3 mm and 0.7 mm respectively from the fuel axis. These thermocouples pass through the interior of the flame, hence measures the fuel vapour temperature, which are less than temperature at flame surface. As TC2 and TC3 pass over the flame surface close to the tip, highest temperatures of around 1500°C are recorded.

Further downstream of the flame tip, the temperature reduces with further increase in the axial distance. In Fig 12(b) the temperature variation along the axis parallel to fuel rod at radial distances of 1.5 mm and 2.3 mm from the centre of the fuel rod is shown for a spreading flame in microgravity. Here, unlike normal gravity where single thermocouple measure the entire axial temperature profile, temperature data from multiple thermocouples at same radial location and from multiples tests are combined together (as explained earlier) to obtain the axial variation of temperature. It may be noted here that the measured temperature in the flame at two different radial position show little difference in the flame temperature. This may be due to fuel jets from bursting bubbles. The maximum recorded temperature at the flame surface is around 1300°C.

Note that the measured temperatures reported here are raw and have not been corrected for radiation loss. The main purpose for the temperature measurement here is to obtain the preheat length ahead of the spreading flame. In the experimental study of Fernandez Pello and Santoro [12] for 1.6 mm diameter PMMA rods it was determined that preheat length in the gas phase extends to a distance which is of same order as in the solid. In the present study the preheat length is determined as the upstream distance from the leading edge of the flame, to the point where the gas temperature in the vicinity of the solid fuel rises to 30°C from the ambient temperature of 25°C. In normal gravity (Fig. 12(a)), the preheating happens over a shorter distance. For the thermocouples placed at 0.7 mm, 1.3 mm and 1.8 mm radial distances the preheat length is about 3.73 mm, 3.11 mm, and 3.49 mm respectively. The variation is about 9% and the average preheat length is taken as 3.44 mm. In microgravity (Fig. 12(b)) the thermocouple placed at radial distances of 1.7 mm and 2.5 mm yielded preheat lengths of 9.97 mm and 9.66 mm respectively and are quite close (within 2%). The average value of 9.82 mm is taken as preheat length of microgravity self-spreading flame over 1 mm diameter fuel at 21% oxygen level.

Based on scaling analysis, the preheat length ( $l_{ph}$ ) for opposed flow flame spreading along thermally thin fuels is the gas phase conduction length scale in axial direction. In microgravity, this is given by  $l_{ph} = \frac{\alpha_g}{V_r}$  where  $\alpha_g$  is the gas phase thermal diffusivity and  $V_r = U_\infty + V_f$ , is the relative velocity at which flow approaches the leading edge of the flame. Here,  $U_\infty$  is the externally imposed opposed speed and  $V_f$  is the flame spread rate. For quiescent flame spread in microgravity,  $U_\infty$  is 0 cm/s and therefore,  $l_{ph} = \frac{\alpha_g}{V_f}$ . For flame spread over 1 mm diameter PMMA rod in quiescent microgravity environment of 21% oxygen,  $V_f$  is about 1.65 mm/s and

therefore, the preheat length estimate is  $l_{ph} = 7$  cm, which is clearly an over estimation of the measured preheat length (here about 1 cm). This also suggests need for redefining of the reference velocity. In quiescent environment a velocity scale apart from the flame spread rate is the Stefan velocity (the velocity at which the fuel vapour comes out of fuel at surface of solid fuel) or air velocity induced due to the Stefan flow.

The estimate of Stefan flow velocity,  $V_{wall}$  can be obtained from the mass burning rate (mass flux,  $\dot{m}_F''$ ) relation [2, 30-32] as  $V_{wall} = \dot{m}_F''/\rho_F$ . Here  $\rho_F$  is the density of the fuel vapor at pyrolysis temperature.

$$\frac{\dot{m}_F''}{\rho_F} = V_{wall} = \frac{h_{eff}}{\rho_F C_{pg}} [1 + B] \quad (1)$$

In the above equation  $h_{eff}$  is the effective heat transfer co-efficient and  $C_{pg}$  is the gas phase specific heat (1.2 kJ/kg K for air), and B is the mass transport number which in a generic form [30] can be written as

$$B = \frac{(1 - \chi) \frac{Y_{0\infty} \Delta H_c}{\nu_s} + C_{pg} (T_\infty - T_v)}{\Delta H_p + Q_{losses}} \quad (2)$$

Here,  $\chi$  is the fraction of the total energy released by the flame that is radiated to the environment,  $Y_{0\infty}$  is the ambient oxygen mass fraction,  $\Delta H_c$  is the heat of combustion (26.4 MJ/kg for PMMA),  $\nu_s$  is the oxygen to fuel ratio (1.92 for PMMA) and  $\Delta H_p$  is the enthalpy of pyrolysis (2 MJ/kg for PMMA). The normalized non-convective heat transfer at the surface represented by  $Q_{losses}$  accounts for in-depth conduction loss, surface re-radiation loss and radiative feedback from the flame and therefore, difficult to obtain analytically. Considering adiabatic and extinction conditions, the B-number can vary between adiabatic B-number to critical B-number [30]. Here for PMMA, adiabatic B-number is about 1.36 and the critical B number is taken as 1 [31].

The effective heat transfer co-efficient is obtained from the correlation  $h_{eff} = C \frac{k_g}{R} [Re^4 + Gr^2]^{\frac{1}{8}} Pr^{\frac{1}{3}}$ , adopted by M. Thomsen *et al.* [32] for burning PMMA rods in normal gravity following the work of Mao *et al.* [33] on convective burning of PMMA in under mixed convection. In the above equation C is a numerical constant,  $Re$  is the Reynolds number ( $= U_f d / 2\nu$ ),  $Gr$  is the Grashof number ( $= g\beta(T_v - T_\infty)R^3 / \nu^2$ ), and  $Pr$  is the Prandtl number

(0.7 for air) .  $U_f$  is the forced flow speed,  $\nu$  is the kinematic viscosity (0.00018 m<sup>2</sup>/ s),  $g$  is the acceleration due to gravity (9.81 m/s<sup>2</sup>),  $\beta = 1/T_\infty$ , is the thermal expansion co-efficient,  $T_v$  is the pyrolysis temperature of PMMA (670K), and  $T_\infty$  is the ambient temperature (300K). For the assumed value of  $C = 1.5$ , Stefan velocity is obtained by iterative solution method and is about 2.01 cm /s for  $B= 1.36$  and 1.31 cm/s for  $B= 1$ . The corresponding preheat lengths are around 1.24 cm and 1.89 cm respectively which are reasonably close to the measured length. Therefore, including Stefan velocity in the definition of the reference velocity,  $V_r = \sqrt{V_B^2 + (V_{wall} + U_\infty + V_f)^2}$  will adequately describe the preheat length scale for a quiescent flame spread in microgravity. Here,  $V_B$  is the magnitude of buoyant velocity. In quiescent microgravity,  $V_r = V_f + V_{wall}$ . Without  $V_{wall}$  the reference velocity is the flame spread rate and the preheat length is grossly over predicted.

#### 4.3 Effect of oxygen concentration on flame spread

To explore the flame spread phenomena at elevated oxygen levels, experiments are conducted at two higher oxygen concentrations (23% and 40%), for 1 mm diameter fuel rods in both normal gravity and microgravity environments, and for various external flow speeds. It may be recalled that the combustion tunnel is placed inside a 44 l polycarbonate enclosure. Initially, a calculated the amount of pure oxygen is added to the enclosure containing dry air. The uniformity of the mixture is ensured by circulating the gases in the enclosure through the mesh layers by turning on the fan located at the entrance of the combustion duct. To monitor oxygen level of the gas mixture and to ensure the gas mixture is uniform, a portion of gas mixture is extracted out of the enclosure using a vacuum pump at the rate of 12 lpm and passed through a portable oxygen analyser (Artech-OIP-03/E, least count 0.1%) at a rate of 2 lpm on a bypass stream before merging with the main stream and returning it back to the enclosure. The depletion in oxygen level after completion of test is also measured to assess the oxygen consumption in the enclosure. In a typical test with initial oxygen level of 23%, the final oxygen level measured after complete combustion of a 70 mm long, 1 mm diameter PMMA rod fuel is 22.9%. Hence, oxygen level may be assumed to be constant during all the tests. The theoretical estimate of the oxygen consumption assuming complete combustion of the same PMMA rod yields a final oxygen level of 22.15%. The difference may be due to incomplete combustion and least count limitation.

Figure 13 shows the instantaneous images of spreading flame over 1 mm diameter fuel rod at 23% and 40% oxygen levels exposed to external flow speeds of 0 cm/s, 10 cm/s, and 25 cm/s in normal gravity and microgravity environments. At oxygen level of 23% the flame shape and trends with flow speed appear similar to ones at 21% oxygen level except that the flames are larger in size and brighter.

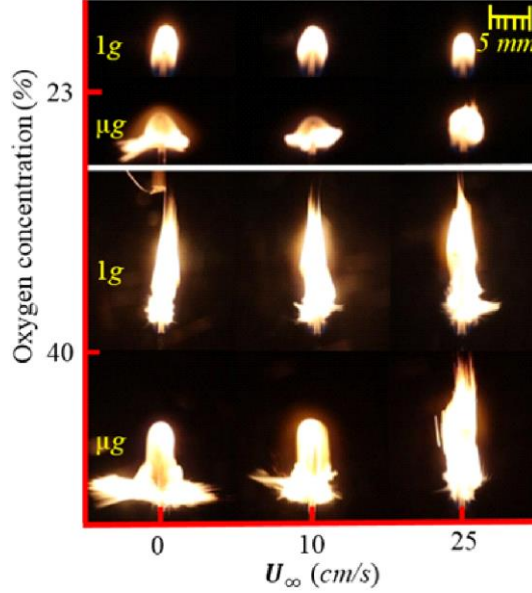


**Fig. 13.** Instantaneous front view images of spreading flame along PMMA rods of diameter 1 mm at 23% and 40% oxygen concentrations in normal gravity and micro-gravity at various opposed flow speeds.

However, at 40% oxygen level, the flames look very different in both normal gravity and microgravity compared to flames at 21% and 23% oxygen levels. The flames are immensely bright and marked with intense fluctuation. The flames are much longer and wider compared to flames of corresponding gravity and flow conditions at near ambient oxygen levels. The length of the pyrolysing segment of fuel in the downstream of the flame leading edge is also much longer at 40% oxygen.

It is interesting to note that in normal gravity as the external flow speed is increased the flame height, flame width, and fluctuations do not appear to change. However, in microgravity, at low external flow speeds, the flame leading edge is bright and fluctuates as a consequence of bursting bubbles at the fuel surface, and the trailing flame segment appears less bright and orange in colour, smooth and length extends over the long fuel pyrolysis segment. As the flow speed is increased, the distortion of flame shape at leading edge due to of fuel jets diminishes and flame length increases and almost appear like a normal gravity flame at 40% oxygen.

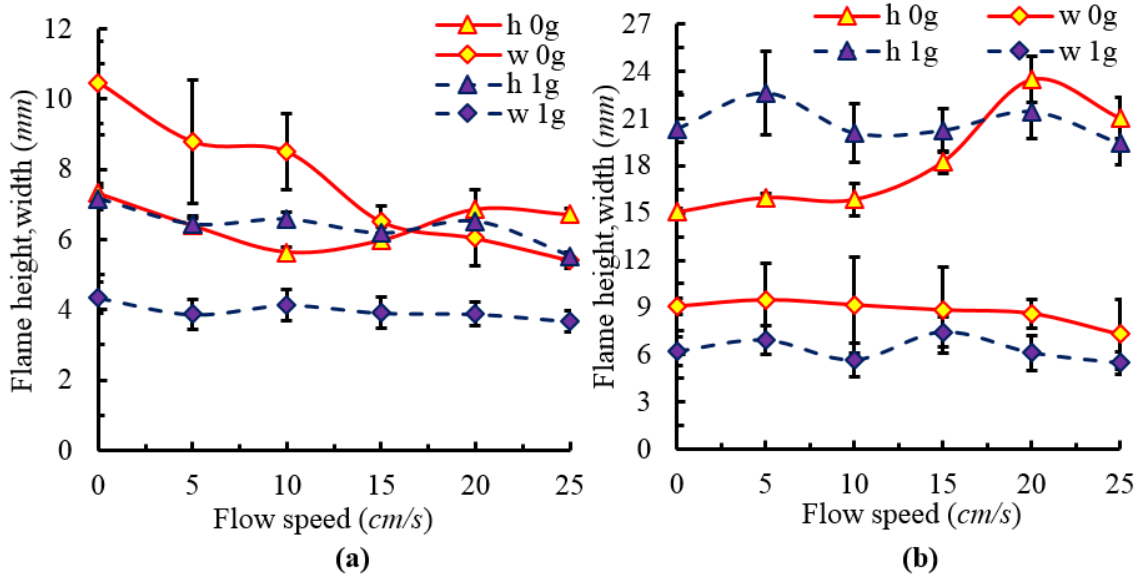


**Fig. 14.** Flame height and width variation with flow speed for 1 mm PMMA cylinders at normal and microgravity (a) 23% of oxygen concentration, (b) 40% of oxygen concentration.

Figure 14 shows the variation of flame height (h), and flame width height (w), with flow speed in both normal gravity and microgravity for a flame spreading over 1 mm diameter fuel rods at 23% (Fig. 14(a)) and 40% (Fig. 14(b)) oxygen concentrations. Similar to Fig. 8 for 21%  $O_2$ , the solid lines represent the microgravity flame dimensions and dashed lines represent normal gravity flame dimensions. At 23% oxygen concentration the overall flame size trend with flow speed is similar to those for flames spreading along 1 mm diameter fuel rods at 21% oxygen. However, the flame aspect ratio (h/w) value ranges with flow speed are different. In normal gravity the flame aspect ratio for the flow speed of 0 cm/s is 1.65 and it decreases slightly to 1.5 at flow speed of 25 cm/s. Note that the decrease is much more steeper with flow for 21%  $O_2$ . In microgravity, the variation in flame aspect ratio with flow speed is significant, from 0.69 for no flow condition to 1.24 (h/w>1) for the flow speed of 25 cm/s. At still higher flow speeds, the aspect ratio of flame is expected to reduce to close to unity, as is the trend for the normal gravity flame.

It is interesting to note that at 40% oxygen concentration, both in normal gravity and microgravity, the flame widths and heights are significantly longer and wider than the corresponding flames for 1 mm fuel diameter at 21% and 23% oxygen concentrations. The spreading flames aspect ratio, h/w are also significantly greater than unity for both normal gravity and microgravity flames. In microgravity, the flame aspect ratio for no flow speed is 1.66 and becomes 2.88 for the flow speed of 25 cm/s. In normal gravity, the flame aspect ratio

practically remains constant (varies from 3.27 at no external flow condition to 3.57 for the flow speed of 25 cm/s).

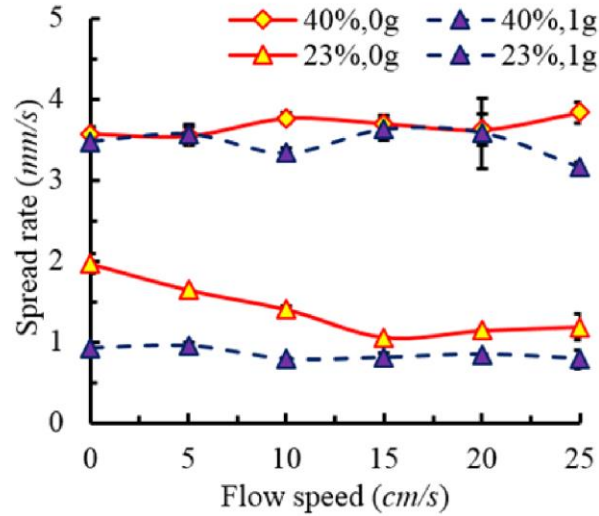


**Fig. 15.** Variation of flame spread rate with flow speed at normal and microgravity at 23% and 40% oxygen levels.

The variation of the flame spread rate with flow speed for 1 mm fuel diameter at 23% and 40% of oxygen levels in normal gravity and micro gravity conditions is shown in Fig. 15. At 23% of oxygen concentration, the flame spread rates are little higher than the flame spread rate values for 21% oxygen (shown in Fig. 9) and have decreasing trend with increase in flow speed in both normal gravity and microgravity. The microgravity flame spread rates are also higher than corresponding normal gravity flame spread rates, with larger difference at low flow speed. However, in the case of 40% oxygen level, it is interesting to note that the flame spreads at a rate of around 3.5 mm/s in both normal gravity and microgravity for all external flow speeds up to 25 cm/s. This characteristic is typical of turbulent jet diffusion flames. Since microgravity flames and normal gravity flames seem to exhibit similar flame spread behaviour at elevated oxygen concentrations, further tests are carried out only in normal gravity for no external flow condition and oxygen levels ranging from 21% to 60%. The tests are conducted for cast PMMA fuel diameters of 0.5 mm and 1 mm.

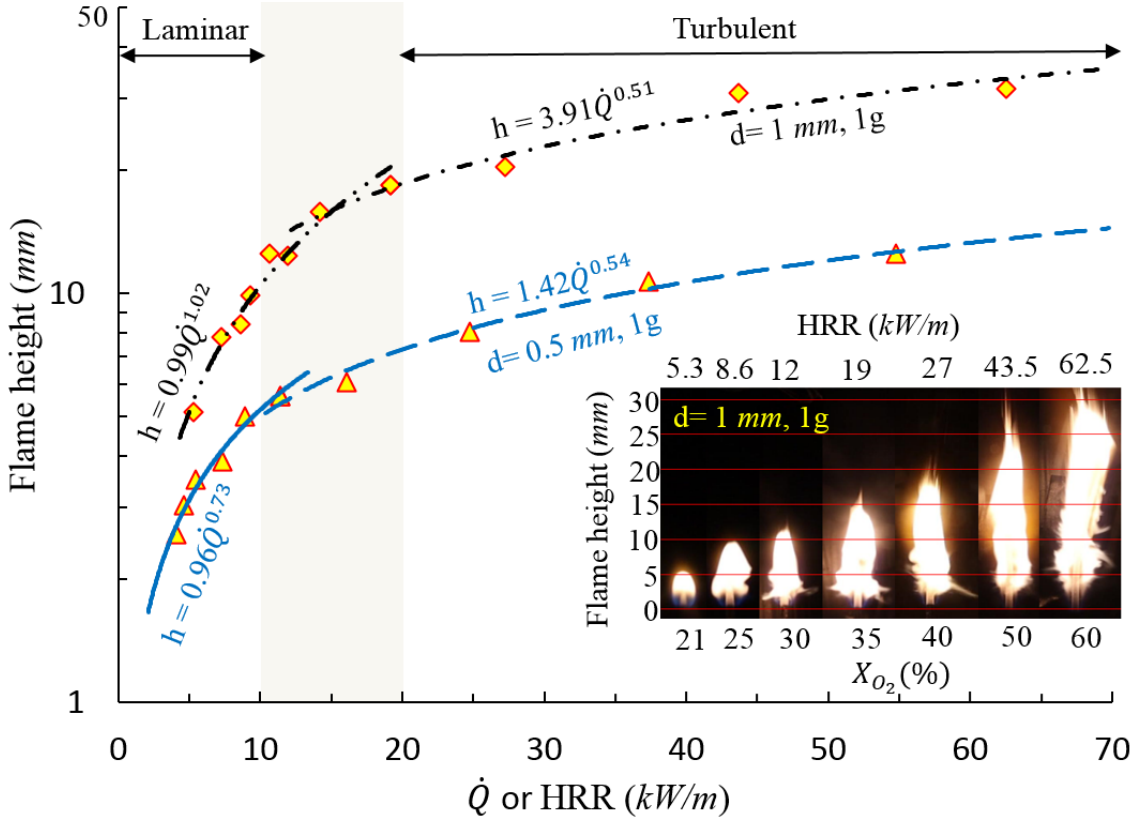


**Fig. 16.** Flame height variation with heat release rate per unit perimeter for PMMA cylinders in normal gravity and microgravity.

Figure 16 shows a plot of flame height ( $h$ ), with heat release rate per unit perimeter (HRR). The HRR values are obtained at each oxygen level using the flame spread rate values as  $\dot{Q} = \eta \Delta H_c A_s \rho_s V_f / P_s$ . Here  $\dot{Q}$  is the HRR,  $\eta$  is the burning fraction (taken 1 for cast PMMA as there is no dripping),  $A_s$  is the cross-section area of the PMMA rod,  $\rho_s$  is density of PMMA (1190 kg/m<sup>3</sup>), and  $P_s$  is the perimeter of the PMMA rod. The flame height increases steeply ( $h \sim \dot{Q}$ ) at low HRR ( $\dot{Q}$ ) values or at low oxygen levels, and less steeply ( $h \sim \dot{Q}^{0.5}$ ) at higher HRR values. The inset of Fig. 16 shows images of flames at various oxygen levels and corresponding HRR values for 1 mm diameter fuel rods. It is observed that the flame is initially laminar at low HRR (or oxygen levels) and appears to become turbulent for HRR ( $\dot{Q}$ ) value between 12 - 19 kW/m (which corresponds to oxygen levels of about 30-35%). In an earlier study on opposed flow and concurrent flow flame spreads along PE coated wires [22], the flames were seen to be laminar in opposed flow configuration and turbulent in concurrent flow configuration. The opposed flow flame height increased steeply with HRR up to a maximum of 30 kW/m and turbulent concurrent flame height exhibited a less steep increase with HRR, starting from value of about 30 kW/m. In upward flame spread studies over walls PMMA [27, 28] and corrugated

cardboard [29] the flame transitions from laminar to turbulent as it grows. The laminar flame height increases steeply with flame wattage and transitions to a turbulent flame where the flame height versus flame wattage curve has a shallow positive slope. The laminar to turbulent transition was noted at about 20-30 kW/m.

Here, in the present study we note that the spreading flame in an opposed flow configuration is laminar at low oxygen levels and turbulent at high oxygen concentrations. The transition from laminar to turbulent flame occurs at lower value of HRR (12-19 kW/m), this may be due to fuel jet issuing out of bursting bubbles at the surface of PMMA rods.

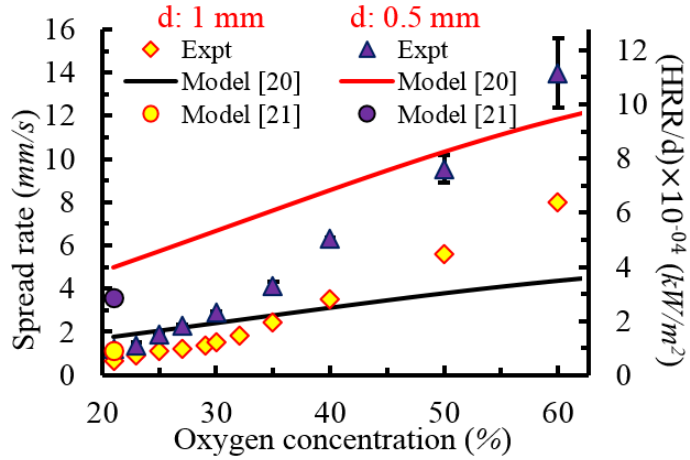


**Fig. 17.** Variation of downward flame spread rate with oxygen concentration and corresponding heat release rate for 1 mm and 0.5 mm diameter PMMA rods.

The variation of the flame spread rate in normal gravity with oxygen concentration for 0.5 mm and 1 mm diameter fuel rods is shown in Fig. 17. The flame spread rate appears to increase linearly with oxygen concentration with an increase of slope for oxygen concentrations above 30-35%, for which the flames are turbulent. Also shown in the figure are predictions of the analytical models of Delichatsios, *et al.* [20] and Bhattacharjee and Delzeit [21]. Note that the model of Delichatsios, *et al.* [20] assumes thermally thin fuel and a laminar flame. Although the model over predicts the flame spread rate values [20], the slope of line is in close agreement with the flame spread rate data of present experiments at low oxygen levels. Note that the slope of 0.5 mm diameter fuel rod is steeper than that for 1 mm fuel rod is also captured by the model. As the model is for a laminar flame, the slope for the experimental turbulent flame spread rate show distinct departure from the predicted laminar flame spread rate slope. The flame spread rates obtained using the thin fuel model of Bhattacharjee and Delzeit [21] and available thermo-

physical property data at 21% oxygen is in reasonably good agreement of the present experimental data. Both 1 mm and 0.5 mm diameter fuel rods are thermally thin [21].

For thin cylindrical fuel rod the flame spread rate is directly proportional to total heat feedback to the fuel surface in the preheat region and therefore,

$$V_f = \frac{2\dot{q}''L_g}{d_0\rho_sC_s(T_v - T_\infty)} \quad (3)$$

Here  $\dot{q}''$  is the average conduction heat flux from flame to preheat length,  $L_g$  is the gas phase thermal length scale,  $d$  is the diameter of fuel rod,  $C_s = 1465 \text{ J/kg K}$  is the specific heat of PMMA,  $T_v = 670 \text{ K}$  is the pyrolysis temperature of PMMA, and  $T_\infty = 300 \text{ K}$  is the ambient temperature. Note that the denominator is practically a constant and the variation in  $V_f$  is due to total heat feedback, ( $\dot{q}''L_g = Z = 0.5V_f d\rho_s C_s(T_v - T_\infty)$ ). Note that for a given fuel diameter here the change in  $V_f$  is due to change in oxygen level. We can define a reference flame spread rate at a reference thermally thin fuel of diameter  $d_0$ , such that total heat feedback to the fuel in the preheat region is  $(\dot{q}''L_g)_0 = Z_0 = 0.5V_{f,0}d_0\rho_s C_s(T_v - T_\infty)$ . Therefore,

$$\bar{Z}(X_{O_2}) = \frac{Z}{Z_0} = \frac{V_f d}{V_{f,0}d_0} \quad (4)$$

$$V_f(X_{O_2}, d) = \bar{Z}(X_{O_2}) V_{f,0} \frac{d_0}{d} \quad (5)$$

In Fig. 18(a) the total heat feedback to the fuel surface of 1 mm diameter fuel rods normalized by reference flame spread rate value at 21% (i.e.  $\bar{Z} = \frac{V_f}{V_{f,0}}$ ) for the same diameter rod, is plotted with oxygen percentage. As pointed out before, in Fig. 17 as there are two regimes of flame spread, laminar and turbulent, with transition point at about 30% oxygen. It is interesting to note a near liner variation of  $\bar{Z}$  with oxygen percentage with a slope change at about 30% oxygen. The slope is steeper in the turbulent regime (at higher oxygen levels). Figure 18(b) shows variation of flame spread rates scaled to the diameter,  $V_f(X_{O_2}, d) \left(\frac{d}{d_0}\right)$  for thermally thin fuels of diameters 0.5 mm, 1 mm from the present work and 1.5 mm, 2 mm and 2.5 mm from [6]. Also plotted in the figure are straight lines corresponding to  $\bar{Z}(X_{O_2}) V_{f,0}$ . The flame spread rate data closely follow the trend line.

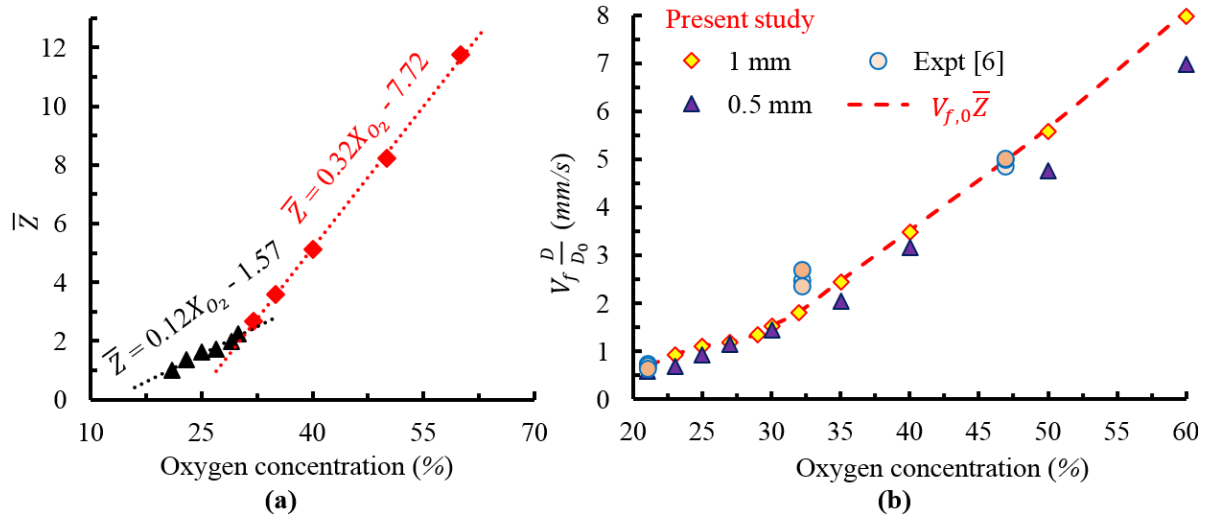
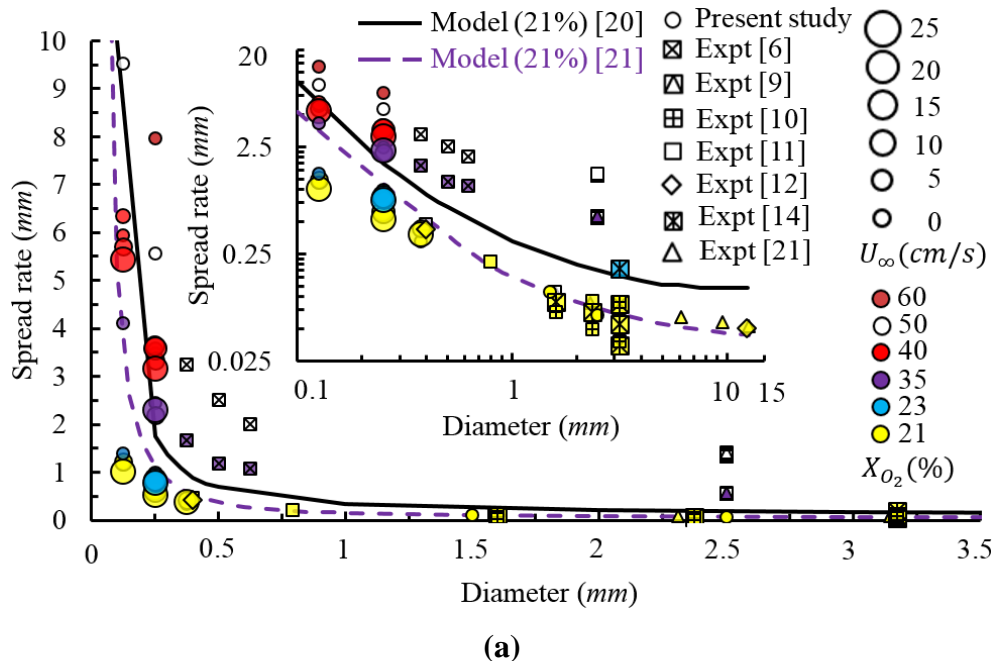


**Fig. 18.** (a) Variation of  $Z$  with oxygen concentrations, (b) Flame spread variation with oxygen concentrations and comparison of modified flame spread model at quiescent normal gravity condition.

#### 4.4 Past and present flame spread rate data along cylindrical PMMA rods



(a)

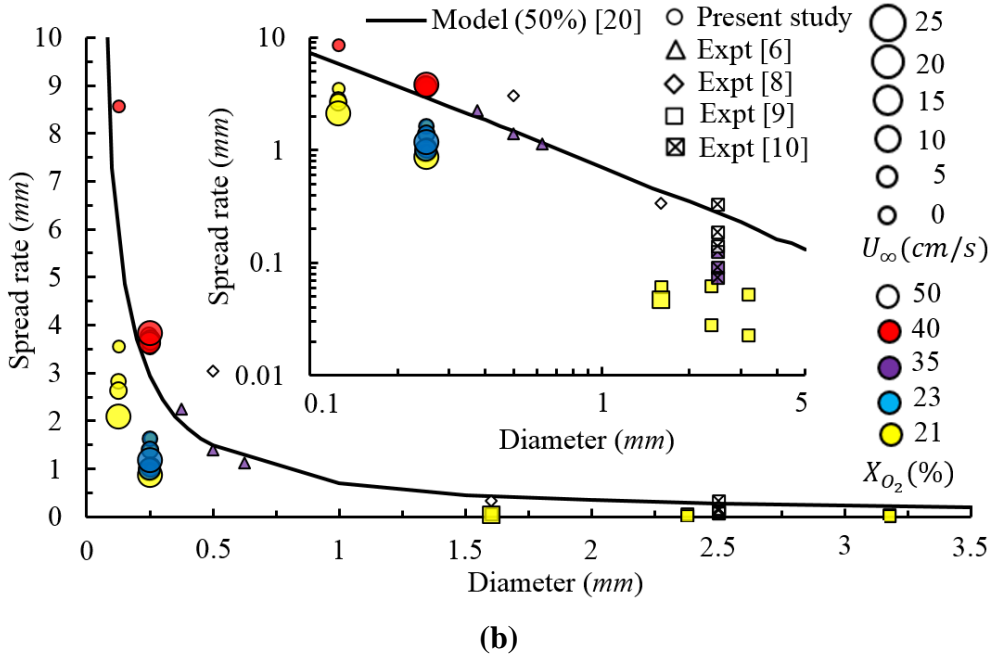


**Fig. 19.** Flame spread rate variation with fuel diameter of PMMA rod at various flow speeds and oxygen concentrations (a) in normal gravity, (b) in microgravity.

Lastly, in this section, the flame spread rates obtained in the present work for both normal gravity and microgravity environments are plotted with fuel diameter for various oxygen levels and flow speeds (see Fig. 19). Also shown in Fig. 19 are the flame spread data for PMMA rods from the previous works [6, 8-12, 14, 20, 21]. The data of the present work are represented by ‘circle’ symbol are located in the left part of the plot contributes to the flame spread data for most thin fuel rods experimented so far. The size of the symbols in the plot reflect the magnitude of the opposed flow speed and the colour of the symbols indicate the oxygen concentration at which the experiments were conducted. Also shown in the figure the curves representing analytical predictions of thin model of Delichatsios, *et al.* [20] and thermally thin and thick models of Bhattacharjee and Delzeit [21] (only for normal gravity) for specific oxygen levels indicated in the figures.

## 5. Conclusions

In the present work, opposed flow downward flame spread experiments are conducted on cast circular PMMA rods of 0.5 mm and 1 mm diameters in both normal gravity and microgravity environments. Flame spread, shape, and behaviour are studied at ambient (21%) and elevated (23%, and 40%) oxygen concentrations in both normal gravity and microgravity environments at various external opposed flow speeds ranging from 0 cm/s to 25 cm/s. Limited set of

experiments are also conducted in normal gravity for no external flow at various oxygen concentrations varying from 21% to 60%. The major findings from the study are as follows,

- 1) The present experimental work contributes to the flame spread data for cast PMMA in normal gravity and microgravity environments for the rods of smallest diameter (1 mm and 0.5 mm) so far in thermally regime. Such data have are difficult to obtain due to fabrication challenges.
- 2) At low oxygen levels (here 21% and 23%) in normal gravity environment the spreading flame is laminar. While in the microgravity environment, the flame acquires the shape of a mushroom with distorted leading edge because of sporadic fuel jets emanating from the bursting bubbles in the solid fuel. This mushroom shape flame is very different from the round shape flame reported in past works on large diameter cylindrical PMMA rods.
- 3) At low oxygen levels (here 21% and 23%), for both fuel rod diameters of 0.5 mm and 1 mm the flame spreads faster in microgravity at all external flow speeds compared to corresponding condition in normal gravity. This is due to longer preheat length in microgravity. Further, the flame spread rate decreases with increase in the external opposed flow speed in both normal gravity and micro gravity environments. This trend is different from the non-monotonic flame spread variation with flow speed reported for thicker PMMA rods. The decrease of flame spread rate with external flow speed is steeper in microgravity. At high oxygen levels, (here 40%) the flame spread rates in normal gravity and microgravity are nearly same at all external flow speeds.
- 4) The sectional view of partially burnt 1 mm PMMA rod under microscope showed bubbles all over the pyrolysis and preheat segments. Numerous small bubbles near the surface and fewer larger bubbles within the solid are noted. The bubbles formed in microgravity appear bigger (50-280  $\mu\text{m}$ ) compared to those formed in normal gravity (40-180  $\mu\text{m}$ ). The measured solid cone half angle (or regression angle) of the pyrolysis segment is about  $7^\circ$  in normal gravity and about  $1.5^\circ$  in microgravity.
- 5) The preheat segment length for spreading flame over 1 mm PMMA rod at 21% oxygen and no external flow condition was determined by temperature measurement using fine thermocouples. The preheat length in microgravity is found to be longer (9.82 mm) compared to the preheat length of normal gravity (3.44 mm). It is shown here that

reasonable theoretical estimate of this preheat length, especially in quiescent microgravity requires Stefan velocity to be included in defining the reference velocity.

- 6) The laminar flame in normal gravity is seen to transition to a turbulent flame at oxygen level of about 30-35%. The flame spread rate curve with oxygen has shallower slope ( $\frac{V_f}{V_{f,0}} = 0.12X_{O_2}$ ) for oxygen below 30% and much steeper slope ( $\frac{V_f}{V_{f,0}} = 0.32X_{O_2}$ ) for oxygen level above 35%. The analytical model in literature which are essentially for laminar flames predict the flame spread rate a low oxygen reasonably well but deviation increases at oxygen level above 35%. At high oxygen level, the flame spread rate becomes insensitive to both gravity and external flow speeds. It is to be noted that the distortion and fluctuation in flame shape due bursting bubbles at the fuel surface is typical of thin fuels as ones studied here and not prominent in thicker fuels.
- 7) The increase in oxygen concentration also increases the flame height. The flame height grows steeply with oxygen level at concentration below 30% and less steeply for oxygen concentration above 35%. The flame height plotted with heat release rate shows a near linear increase ( $h \sim \dot{Q}$ ) at low oxygen and a weaker dependence at higher oxygen levels ( $h \sim \dot{Q}^{0.5}$ ). This behaviour is typical of a jet diffusion flame in laminar and turbulent regimes.

## References

- [1] D.L. Urban, P. Ferkul, S. Olson, G.A. Ruff, J. Easton, J.S. T'ien, Y.T. Liao, C. Li, C. F. Pello, J.L. Torero, G. Legros, C. Eigenbrod, N. Smirnov, O. Fujita, S. Rouvreau, B. Toth, G. Jomaas, Flame spread: effects of microgravity and scale, *Combust. Flame* 199 (2019) 168–182.
- [2] J.G. Quintiere, *Fundamentals of Fire Phenomena*, John Wiley & Sons, West Sussex, England, 2006.
- [3] A.C. Fernandez-Pello, T. Hirano, Controlling mechanisms of flame spread, *Combust. Sci. Technol.* 32 (1983) 1–31.
- [4] I.S. Wichman, Theory of opposed-flow flame spread, *Prog. Energy Combust. Sci.* 18

(1992) 553–593.

- [5] X. Huang, J. Gao, A review of near-limit opposed fire spread, *Fire Saf. J.* 120 (2021) 103141.
- [6] C. S. Tarifa, A. L. Martinez, J.J. Salva Monfort, G.L. Juste, J.M. Tizon Pulido, J.M. Cura Velayos, *Study on combustion processes in reduced gravity, Volume 1*, Polytechnic University of Madrid, Spain, 1990.
- [7] M. F. Bundy, *A Computational Model for Flame Spread along Cylindrical Fuels in a Microgravity Environment* (Ph.D. thesis), Washington State University, Pullman, Washington, USA, 1998.
- [8] L. Carmignani, S. Sato, S. Bhattacharjee, Flame spread over acrylic cylinders in microgravity: effect of surface radiation on flame spread and extinction, *48th International Conference on Environmental Systems* (2018), paper 311.
- [9] S. Link, X. Huang, C. Fernandez-Pello, S. Olson, P. Ferkul, The effect of gravity on flame spread over pmma cylinders, *Sci. Rep.* 8 (2018) 2–10.
- [10] C. Wu, X. Huang, S. Wang, F. Zhu, Y. Yi, Opposed flame spread over cylindrical PMMA under oxygen-enriched microgravity environment, *Fire Technol.* 56 (2020) 71–89.
- [11] M. Sibulkjn, C.K. Lee, Flame propagation measurements and energy feedback analysis for burning cylinders, *Combust. Sci. Technol.* 9 (1974) 137–147.
- [12] A.C. Fernandez-Pello, R.J. Santoro, On the dominant mode of heat transfer in downward flame spread, *Symp. (Int.) Combust.* 17 (1979) 1201–1209.
- [13] X. Huang, S. Link, A. Rodriguez, M. Thomsen, S. Olson, P. Ferkul, C. Fernandez-Pello, Transition from opposed flame spread to fuel regression and blow off: Effect of flow, atmosphere, and microgravity, *Proc. Combust. Inst.* 37 (2019) 4117–4126.
- [14] M. Thomsen, C. Fernandez-Pello, X. Huang, S. Olson, P. Ferkul, Buoyancy effect on downward flame spread over pmma cylinders, *Fire Technol.* 56 (2020) 247–269.
- [15] M. Thomsen, C. Fernandez-Pello, X. Huang, S.L. Olson, P. V. Ferkul, Opposed flow burning of PMMA cylinders in normoxic atmospheres, *Fire Saf. J.* 110 (2019) 102903.

- [16] O. Korobeinichev, A. Shmakov, K. Osipova, A. Kumar, and K. Naresh, Experimental study and numerical modeling of downward flame spread along a single pine needle: Part 1 (Experiments), *Combust. Sci. Technol.* 190 (2018) 164–185.
- [17] K. Naresh, A. Kumar, O. Korobeinichev, A. Shmakov, and K. Osipova, Downward flame spread along a single pine needle: Numerical modelling, *Combust. Flame* 197 (2018) 161–181.
- [18] J. C. Yang, A. Hamins, M.K. Salva Donnelly, Combustion of a polymer (PMMA) sphere in microgravity, report No. NISTIR 6331, Building and Fire Research laboratory, Gaithersburg, MD, USA, 1999.
- [19] J.N. De Ris, Spread of a laminar diffusion flame, *Symp. (Int.) Combust.* 12 (1969) 241–252.
- [20] M.A. Delichatsios, R.A. Altenkirch, M.F. Bundy, S. Bhattacharjee, L. Tang, K. Sacksteder, Creeping flame spread along fuel cylinders in forced and natural flows and microgravity, *Proc. Combust. Inst.* 28 (2000) 2835–2842.
- [21] S. Bhattacharjee, T. Delzeit, Opposed-flow flame spread over cylindrical fuels: Spread rate formulas and experimental verification, *Proc. Combust. Inst.* 39 (2022) 3863–3870.
- [22] Y. Ma, L Hu, S Jia, J Lv, S Xiong, Analysis of upward- and downward flame spread over vertical installed polyethylene-insulated electrical wires, *Combust. Flame* 238 (2022) 111896.
- [23] Y. Konno, N. Hashimoto, O. Fujita, On the radiation extinction of opposed flame spread over curved solid surface in low flow velocity conditions, *Combust. Flame* 254 (2023) 112836.
- [24] V. V. Nikhil, A. Nair, P. Niketh, A. Kumar, M. Muruganandam, The 2.5 s Microgravity drop tower at national centre for combustion research and development (NCCRD), Indian institute of technology madras, *Microgravity Sci. Technol.* 30 (2018) 663–673.
- [25] N. Otsu, A threshold selection method from gray-level histograms, *IEEE Trans. Syst. Man. Cybern.* 9 (1979) 62–66.
- [26] S.L. Olson, Mechanisms of microgravity flame spread over a thin solid fuel: Oxygen and opposed flow effects, *Combust. Sci. Technol.* 76 (1991) 233–249.

- [27] K.C. Tsai, D. Drysdale, Flame height correlation and upward flame spread modelling, *Fire Mater.* 26 (2002) 279–287.
- [28] K.M. Tu, J.G. Quintiere, Wall flame heights with external radiation, *Fire Technol.* 27 (1991) 195–203.
- [29] M.J. Gollner, F.A. Williams, A.S. Rangwala, Upward flame spread over corrugated cardboard, *Combust. Flame.* 158 (2011) 1404–1412.
- [30] J. L. Torero, T. Vietoris, G. Legros, P. Joulain, Estimation of a total mass transfer number from the standoff distance of a spreading flame, *Combust. Sci. Technol.* 174 (2002) 187–203.
- [31] C. Wu, P. Sun, X. Wang, X. Huang, S. Wag, Flame extinction of spherical PMMA in microgravity: Effect of fuel diameter and conduction, *Microgravity Sci. Technol.* 32 (2020) 1065–1075.
- [32] M. Thomsen, C. Fernandez-Pello, S.L. Olson, P. V. Ferkul, Downward burning of PMMA cylinders: The effect of pressure and oxygen, *Proc. Combust. Inst.* 38 (2021) 4837–4844.
- [33] C. P. Mao, A. C. Fernandez-Pello, P. J. Pagni, Mixed convective burning of a fuel surface with arbitrary inclination, *J. Heat Transf.* 106 (1984) 304–309 .